OBSTACLE-AWARE MULTI-UAV FORMATION COORDINATION VIA A HIERARCHICAL GUIDING VECTOR FIELD WITH ADAPTIVE VIRTUAL COORDINATES

Anonymous authors
Paper under double-blind review

ABSTRACT

This paper presents a hierarchical guiding vector field (HGVF) with adaptive virtual coordinates for multi-UAV formation coordination in a two-dimensional workspace containing known static circular obstacles. The outer layer modifies the original closed path in its normal direction to construct an obstacle-aware path. Based on the estimated obstacle risk, a shared formation variable continuously interpolates the virtual-coordinate offsets and normal offsets between circular and line formation parameters. A distributed virtual-coordinate law regulates the virtual-coordinate differences using neighboring scalar virtual-coordinate information. The inner layer guides each UAV along its individual reference and combines the resulting tracking field with local obstacle and inter-UAV repulsive corrections to generate bounded velocity commands. Numerical comparisons and CoppeliaSim results show positive obstacle clearances, temporary tracking and coordination errors during formation reconfiguration, and transitions between the circular and line configurations in the considered scenario.

1 INTRODUCTION

Multi-unmanned aerial vehicle (multi-UAV) systems improve spatial coverage and task efficiency through coordinated motion Chung et al. (2018); Oh et al. (2015). In obstacle-populated environments, however, path following, formation maintenance, external-obstacle avoidance, and inter-UAV separation become strongly coupled. The problem is more challenging when the formation must also reconfigure according to the encountered obstacle risk: the UAVs must change their relative arrangement without interrupting path progression or distributed coordination.

Existing studies provide strong foundations for formation control, vector-field guidance, and collision avoidance, but usually address different parts of this coupled problem. In particular, guiding vector fields (GVFs) combine path convergence and progression in a geometric feedback law. Yao et al. (2023) extended this idea by treating path parameters as virtual coordinates and coordinating prescribed parametric differences through local communication. Nevertheless, external-obstacle-aware path deformation and risk-driven, time-varying formation offsets are not included in that framework. Conversely, existing reactive, predictive, and reconfigurable formation methods do not jointly provide an obstacle-aware path and distributed adaptive virtual-coordinate coordination.

To bridge this gap, we develop a hierarchical guiding vector field (HGVF) with adaptive virtual coordinates for multi-UAV formation motion along a closed path in a two-dimensional workspace with known static circular obstacles. The outer layer deforms the original path in its normal direction to construct an obstacle-aware path. An obstacle-risk-dependent formation variable continuously interpolates the virtual-coordinate offsets and normal offsets between circular and line formation parameters. The distributed virtual-coordinate coordination term uses neighboring scalar virtual-coordinate information, while the inner layer tracks the individual references and incorporates local obstacle and inter-UAV repulsive corrections into the bounded velocity commands.

Table 1 compares the functions explicitly considered in representative multi-UAV formation methods. The comparison concerns method scope rather than control performance or formal safety guarantees.

Reviewers: please read the Reviewer Guidelines (iclr.cc/Conferences/2027/ReviewerGuidelines) and the AI Policy for Reviewers (iclr.cc/Conferences/2027/AIPolicyForReviewers). If you used AI to expand, edit, or polish your review, please provide the input text to the LLM. Better still, consider skipping the LLM and submitting your original text: we, and the authors, are much more interested in your unedited thoughts than in what an LLM has to say. AI-assisted or not, you are putting your name and reputation behind your review: LLM-generated falsehoods, hallucinations or misrepresentations are subject to disciplinary action, which may include desk-rejecting all papers you have authored.

Table 1: Qualitative comparison with representative multi-UAV formation methods

Study	PT	OA	IS	AR	DC
Proposed method	✓	✓	✓	✓	✓
Ma et al. (2022)	–	✓	△	–	✓
Yu et al. (2024)	–	–	✓	–	✓
Pan et al. (2022)	✓	✓	✓	–	△
Wang & Sun (2019)	–	✓	✓	–	△
Du et al. (2024)	✓	✓	✓	△	✓
Lan et al. (2025)	–	–	–	△	✓
Zhang et al. (2022)	✓	✓	✓	–	✓
Dong et al. (2017)	✓	–	–	–	✓
Yao et al. (2023)	✓	–	✓	–	✓

PT: path following; OA: external-obstacle avoidance; IS: inter-UAV separation; AR: adaptive reconfiguration; DC: distributed coordination. ✓: yes; △: partial; –: no.

Our main contributions are summarized as follows. **(1)** We construct an HGVF that combines an outer obstacle-aware path with inner individual-reference tracking and local obstacle and inter-UAV repulsive corrections. **(2)** We develop an adaptive virtual-coordinate formation coordination mechanism in which the estimated obstacle risk continuously changes the virtual-coordinate offsets and physical normal offsets between circular and line formation parameters. The distributed coordination term requires only scalar virtual coordinates exchanged between neighboring UAVs. Numerical comparisons and CoppeliaSim results evaluate the resulting obstacle-aware formation motion, reference tracking, and virtual-coordinate coordination.

2 Related Work

Formation coordination and reconfiguration. Consensus and flocking provide basic mechanisms for coordinating agents through local interactions Ren & Beard (2005); Olfati-Saber (2006), and have been combined with formation control and path following Reyes & Tanner (2015). Related studies address circular formations, cooperative moving-path following, prescribed-performance formation control, and robustness to heterogeneous uncertainties Sun et al. (2019); Wang et al. (2019); Mehdifar et al. (2020); Yang et al. (2023). Predefined time-varying formations and failure-driven topology and formation reconfiguration are studied in Dong et al. (2017); Lan et al. (2025). These approaches do not, however, use obstacle risk to continuously coordinate both virtual-coordinate offsets and normal offsets.

Guiding vector fields and virtual coordinates. Vector-field guidance has been developed for miniature aerial vehicles, time-varying curves, and nonholonomic robots Nelson et al. (2007); Goncalves et al. (2010); Kapitaniuk et al. (2018), while a singularity-free construction addresses critical points associated with implicit path representations Yao et al. (2021). Most closely related to this work, Yao et al. (2023) coordinate virtual coordinates over a communication graph and include an extension for inter-robot collision avoidance. Their convergence results concern fixed desired parametric differences; here, the desired offsets vary with obstacle risk and the reference path is deformed around obstacles.

Obstacle avoidance in multi-UAV formation motion. Artificial potential fields and vector-field guidance are classical reactive approaches to obstacle avoidance Khatib (1986); Chen et al. (2013). For multi-UAV systems, potential-field and local-planning methods have been combined with consensus, adaptive, leader–follower, or passivity-based formation control Ma et al. (2022); Yu et al. (2024); Pan et al. (2022); Wang & Sun (2019); Zhang et al. (2022). Predictive methods generate collision-aware trajectories Luis & Schoellig (2019); Luis et al. (2020); Alonso-Mora et al. (2015), while safety barrier certificates and control barrier functions impose formal safety conditions Wang et al. (2017); Ames et al. (2017). Distributed model predictive control has also been used for formation tracking–containment with obstacle avoidance Du et al. (2024). These methods motivate

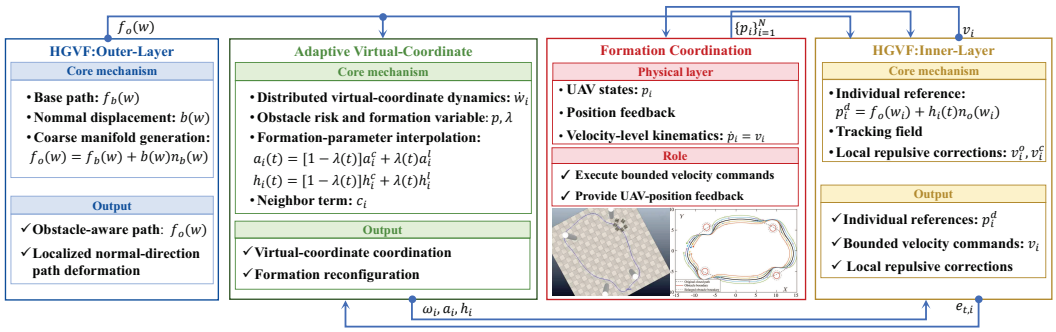


Figure 1: Framework of the proposed HGVF with adaptive virtual-coordinate formation coordination.

the obstacle-handling components of our framework, but do not combine them with the proposed risk-driven virtual-coordinate reconfiguration.

3 METHODOLOGY

This section presents the proposed HGVF with adaptive virtual coordinates. The outer layer constructs an obstacle-aware path by modifying the original closed path in its normal direction. Based on this manifold, the adaptive virtual-coordinate formation coordination mechanism generates the time-varying formation parameters and coordinates the shifted virtual coordinates through neighboring information. The inner layer constructs the individual references and generates the corresponding tracking field. Local obstacle and inter-UAV repulsive corrections are then incorporated into the velocity command. The information flow among the two HGVF layers, adaptive virtual-coordinate formation coordination, and the multi-UAV formation system is summarized in Fig. 1.

3.1 SYSTEM DESCRIPTION AND OUTER-LAYER OBSTACLE-AWARE PATH

Consider a multi-UAV system composed of N UAVs moving in a two-dimensional workspace. Let $\boldsymbol{p}_i = [x_i, y_i]^{\mathrm{T}} \in \mathbb{R}^2$ denote the position of UAV i. Consistent with the velocity-level implementation, the UAV kinematics are described by

$$\dot{\boldsymbol{p}}_i = \boldsymbol{v}_i, \qquad i \in \mathcal{V} := \{1, \dots, N\}, \tag{1}$$

where $\boldsymbol{v}_i \in \mathbb{R}^2$ is the velocity command.

The communication topology is represented by an undirected graph $\mathcal{G} = (\mathcal{V}, \mathcal{E})$, where $\mathcal{E}$ is the edge set. In the current implementation, the UAVs communicate through the cycle graph $\mathcal{E} = \{(1,2), (2,3), \dots, (N-1, N), (N, 1)\}$. The neighbor set of UAV i is denoted by $\mathcal{N}_i$. For virtual-coordinate coordination, each UAV exchanges its scalar virtual coordinate with its neighbors.

The workspace contains M static circular obstacles. Obstacle m is described by

$$\mathcal{O}_m = \left\{\boldsymbol{p} \in \mathbb{R}^2 : \|\boldsymbol{p} - \boldsymbol{c}_m\| \le r_m\right\}, \qquad m \in \mathcal{M} := \{1, \dots, M\}, \tag{2}$$

where $\boldsymbol{c}_m \in \mathbb{R}^2$ and $r_m > 0$ are the center and radius of obstacle m, respectively. Based on (2), an enlarged obstacle boundary is introduced as

$$r_m^b = r_m + d_b, \tag{3}$$

where $d_b > 0$ is the boundary enlargement.

For subsequent design, define the saturation operator as $\mathrm{sat}_{[\underline{s},\overline{s}]}(s) = \min\left\{\max\{s, \underline{s}\}, \overline{s}\right\}$, $\underline{s} < \overline{s}$, and $\mathrm{wrap}(\delta) = \mathrm{mod}(\delta + \pi, 2\pi) - \pi$, where $\mathrm{mod}(\delta + \pi, 2\pi)$ denotes the remainder in $[0, 2\pi)$, so $\mathrm{wrap}(\delta) \in [-\pi, \pi)$.

Let $w \in \mathbb{R}$ denote an unwrapped virtual coordinate associated with the closed path. Although the path satisfies $\boldsymbol{f}_b(w + 2\pi) = \boldsymbol{f}_b(w)$, the virtual coordinate is allowed to increase continuously over

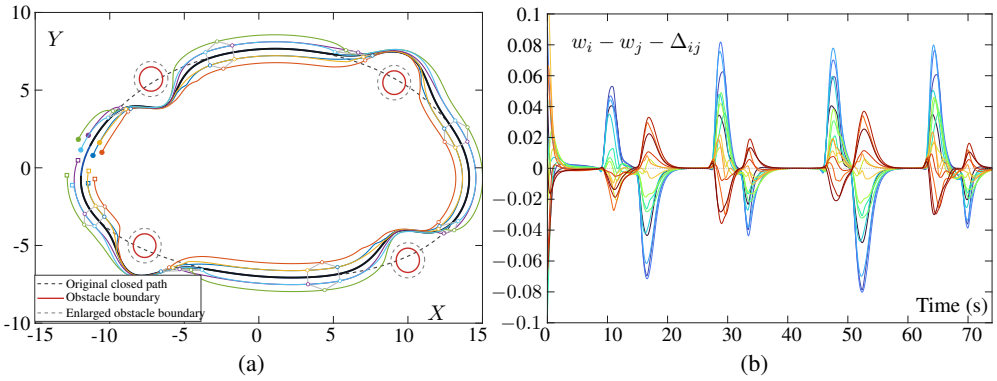


Figure 2: Formation motion and virtual-coordinate coordination. (a) Multi-UAV formation motion along the closed path with static circular obstacles; (b) virtual-coordinate coordination errors of all UAV pairs.

successive path cycles. The original path is parameterized as

$$\boldsymbol{f}_b(w) = \begin{bmatrix} c_x + R_x \cos w + A_x \cos(2w + \phi_x) \\ c_y + R_y \sin w + A_y \sin(2w + \phi_y) \end{bmatrix}, \tag{4}$$

where (c_x, c_y) is the path center, R_x and R_y determine its principal dimensions, and A_x, A_y, ϕ_x, and ϕ_y determine its second-harmonic deformation. This parameterization produces a smooth closed path with moderate geometric variation. The derivative of (4) is

$$\boldsymbol{f}_b'(w) = \begin{bmatrix} -R_x \sin w - 2A_x \sin(2w + \phi_x) \\ R_y \cos w + 2A_y \cos(2w + \phi_y) \end{bmatrix}.$$

The path parameters are chosen such that $\|f_b'(w)\| > 0$ for all w, and the corresponding unit tangent and unit normal vectors are defined by

$$\boldsymbol{t}_b(w) = \frac{\boldsymbol{f}_b'(w)}{\|\boldsymbol{f}_b'(w)\|}, \qquad \boldsymbol{n}_b(w) = \begin{bmatrix} -t_{b,y}(w) \\ t_{b,x}(w) \end{bmatrix}.$$

For obstacle m, its corresponding virtual coordinate is selected as $w_m \in \underset{w \in [0, 2\pi)}{\arg\min} \|\boldsymbol{f}_b(w) - \boldsymbol{c}_m\|$.

Assuming that the obstacle center does not lie exactly on the path, its side indicator is $s_m = \operatorname{sgn}\left[\left(\boldsymbol{c}_m - \boldsymbol{f}_b(w_m)\right)^{\mathrm{T}} \boldsymbol{n}_b(w_m)\right] \in \{-1, 1\}$. Thus, $s_m = 1$ and $s_m = -1$ indicate the positive and negative normal sides, respectively.

$$\beta_m(w) = \exp\left[-\frac{1}{2}\left(\frac{\operatorname{wrap}(w - w_m)}{\sigma_m}\right)^2\right], \tag{5}$$

where $\sigma_m > 0$ determines its influence range in the parameter domain.

Based on (5), the total normal displacement is constructed as

$$b(w) = \sum_{m=1}^{M} (-s_m) A_m \beta_m(w), \tag{6}$$

where $A_m > 0$ is the displacement amplitude associated with obstacle m. The factor $-s_m$ causes the path to deform toward the side opposite to the obstacle. The obstacle-aware obstacle-aware path is defined by

$$\boldsymbol{f}_o(w) = \boldsymbol{f}_b(w) + b(w)\boldsymbol{n}_b(w). \tag{7}$$

It follows from (5)–(7) that the obstacle-aware path approaches the original path outside the parameter-domain influence regions, while localized normal deviations are generated near the obstacles. Consistent with the numerical implementation, the derivative of the obstacle-aware path is

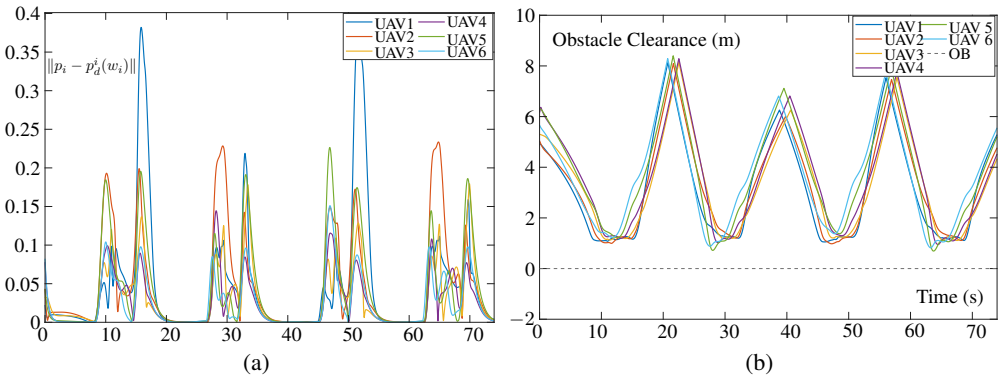


Figure 3: Tracking and obstacle-clearance results. (a) Position-reference tracking errors of the individual UAVs; (b) obstacle clearances of the individual UAVs, where OB denotes the obstacle boundary.

evaluated using the central difference

$$\boldsymbol{f}_o'(w) = \frac{\boldsymbol{f}_o(w+\varepsilon_w) - \boldsymbol{f}_o(w-\varepsilon_w)}{2\varepsilon_w},$$

where $\varepsilon_w > 0$ is a sufficiently small parameter increment. The corresponding unit tangent and unit normal vectors are

$$\boldsymbol{t}_o(w) = \frac{\boldsymbol{f}_o'(w)}{\|\boldsymbol{f}_o'(w)\|}, \qquad \boldsymbol{n}_o(w) = \begin{bmatrix} -t_{o,y}(w) \\ t_{o,x}(w) \end{bmatrix}.$$

3.2 Adaptive Virtual-Coordinate Formation Coordination

The formation geometry is represented by a tangential virtual-coordinate offset and a normal offset. For the circular formation, define

$$\theta_i = \frac{2\pi(i-1)}{N} + \theta_b, \qquad i \in \mathcal{V},$$

where θ_b is a prescribed angular bias. The circular-formation parameters are

$$a_i^c = \frac{R_f}{s_f}\cos\theta_i, \qquad h_i^c = R_f \sin\theta_i, \tag{8}$$

where $R_f > 0$ is the circular-formation radius and $s_f > 0$ is a scaling factor that approximately converts a physical tangential distance into a virtual-coordinate difference.

For the line formation, the formation parameters are selected as

$$a_i^l = \left(i - \frac{N+1}{2}\right)\frac{d_l}{s_f}, \qquad h_i^l = 0, \tag{9}$$

where $d_l > 0$ determines the tangential spacing between adjacent formation members. Therefore, the line formation is approximately aligned with the local tangent direction of the coarse manifold.

Let $\lambda(t) \in [0,1]$ denote the adaptive formation variable. The time-varying formation parameters interpolate between (8) and (9) according to

$$a_i(t) = [1-\lambda(t)]a_i^c + \lambda(t)a_i^l, \qquad h_i(t) = [1-\lambda(t)]h_i^c + \lambda(t)h_i^l. \tag{10}$$

Thus, $\lambda = 0$ corresponds to the circular formation, whereas $\lambda = 1$ corresponds to the line formation. Since $a_i(t)$ represents the desired virtual-coordinate offset of UAV i relative to the formation center, the formation-center virtual coordinate is estimated as

$$\widehat{w}_c = \frac{1}{N}\sum_{i=1}^{N}[w_i - a_i(t)]. \tag{11}$$

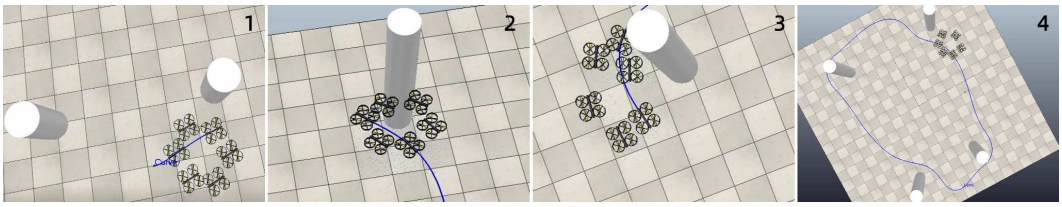


Figure 4: CoppeliaSim snapshots of the multi-UAV formation motion along the closed path with static circular obstacles.

The corresponding estimated formation-center position on the outer manifold is

$$\widehat{\boldsymbol{p}}_c = \boldsymbol{f}_o(\widehat{w}_c). \tag{12}$$

In the current implementation, the aggregate estimate in (11) is evaluated using all virtual coordinates, and the resulting common formation variable $\lambda(t)$ is supplied to all UAVs. The distributed property refers specifically to the neighbor-based virtual-coordinate coordination term introduced below. Based on (11) and (12), the clearance between the estimated formation center and the enlarged boundary of obstacle m is defined as $d_m^b = \|\widehat{\boldsymbol{p}}_c - \boldsymbol{c}_m\| - r_m^b$.

The corresponding distance-based obstacle risk is

$$\rho_{d,m} = \mathrm{sat}_{[0,1]}\left(\frac{R_\rho - d_m^b}{R_\rho}\right), \tag{13}$$

where $R_\rho > 0$ denotes the risk-evaluation range.

To account for the relative position in the parameter domain, define the parameter-based obstacle risk as

$$\rho_{w,m} = \exp\left[-\frac{1}{2}\left(\frac{\mathrm{wrap}(\widehat{w}_c - w_m)}{\sigma_\rho}\right)^2\right], \tag{14}$$

where $\sigma_\rho > 0$ determines the corresponding parameter-domain range. Using (13) and (14), the overall obstacle risk is calculated as

$$\rho = \mathrm{sat}_{[0,1]}\left[\max_{m\in\mathcal{M}}\left\{\max\left(\rho_{d,m}, \kappa_\rho \rho_{w,m}\right)\right\}\right], \tag{15}$$

where $\kappa_\rho \in (0, 1]$ weights the parameter-based risk. In the current implementation, $\kappa_\rho = 0.8$.

Let $0 \le \rho_l < \rho_h \le 1$ denote the lower and upper risk thresholds, respectively. The desired formation variable is generated by $\lambda_d = \mathcal{S}(\rho; \rho_l, \rho_h)$, where

$$\mathcal{S}(\rho; \rho_l, \rho_h) = \begin{cases} 0, & \rho \le \rho_l, \\ 10s_\rho^3 - 15s_\rho^4 + 6s_\rho^5, & \rho_l < \rho < \rho_h, \\ 1, & \rho \ge \rho_h, \end{cases} \qquad s_\rho = \frac{\rho - \rho_l}{\rho_h - \rho_l}. \tag{16}$$

The fifth-order polynomial in (16) provides a smooth transition between the circular and line formations. The adaptive formation variable evolves according to

$$\dot{\lambda} = k_\lambda(\lambda_d - \lambda), \tag{17}$$

where $k_\lambda > 0$ determines the formation-reconfiguration rate. In the discrete implementation, it is updated by

$$\lambda(t_{k+1}) = \mathrm{sat}_{[0,1]}\left[\lambda(t_k) + \Delta t\, k_\lambda\big(\lambda_d(t_k) - \lambda(t_k)\big)\right].$$

Therefore, the formation gradually changes from the circular configuration to the line configuration as the obstacle risk increases and returns to the circular configuration after the obstacle risk decreases. For UAV i, an individual parametric reference is generated by shifting the obstacle-aware path along its local normal direction:

$$\boldsymbol{p}_i^d(w_i, t) = \boldsymbol{f}_o(w_i) + h_i(t)\boldsymbol{n}_o(w_i). \tag{18}$$

Table 2: Quantitative comparison with baseline methods.

Method	$d_{o,\min}$	$d_{b,\min}$	$d_{u,\min}$	RMSE_p	RMSE_c
Proposed method	**0.69982**	**0.34982**	0.27870	**0.094973**	0.17126
VAPF	0.50232	0.15232	0.30741	0.34976	0.24846
Improved APF	−0.092619	−0.44262	**0.58428**	0.14314	**0.12632**

For compactness, let $\boldsymbol{f}_i(w_i,t) := \boldsymbol{p}_i^d(w_i,t)$. In (18), the tangential formation arrangement is represented by the virtual-coordinate offset $a_i(t)$, whereas the normal formation arrangement is directly represented by $h_i(t)$. Consistent with the numerical implementation, the derivative of the individual reference with respect to w_i is evaluated as

$$\boldsymbol{f}_i'(w_i,t) = \frac{\boldsymbol{p}_i^d(w_i+\varepsilon_w,t) - \boldsymbol{p}_i^d(w_i-\varepsilon_w,t)}{2\varepsilon_w}. \tag{19}$$

The formation and manifold parameters are selected such that $\|\boldsymbol{f}_o'(w)\| > 0$ and $\|\boldsymbol{f}_i'(w_i,t)\| > 0$ over the considered trajectories. Based on (19), the corresponding unit tangent vector is

$$\boldsymbol{t}_i(w_i,t) = \frac{\boldsymbol{f}_i'(w_i,t)}{\|\boldsymbol{f}_i'(w_i,t)\|}.$$

Define the position-reference tracking error as

$$\boldsymbol{e}_i = \boldsymbol{p}_i - \boldsymbol{p}_i^d(w_i,t). \tag{20}$$

Using (20), its tangential component is defined as

$$e_{t,i} = \boldsymbol{e}_i^{\mathrm{T}} \boldsymbol{t}_i(w_i,t). \tag{21}$$

The virtual coordinate w_i specifies the location of the individual reference point of UAV i on its parametric reference. For any distinct $i,j \in \mathcal{V}$, the desired parametric difference is defined as

$$\Delta_{ij}(t) = a_i(t) - a_j(t). \tag{22}$$

The virtual-coordinate coordination error is given by

$$e_{ij}^w = w_i - w_j - \Delta_{ij}(t). \tag{23}$$

Substituting (22) into (23) yields

$$e_{ij}^w = [w_i - a_i(t)] - [w_j - a_j(t)]. \tag{24}$$

Since $\Delta_{ij}(t) = a_i(t) - a_j(t)$, the desired differences are consistent around the cycle graph, and reducing (24) aligns the formation-center virtual coordinates. The distributed coordination term for UAV i is designed as

$$c_i = -\sum_{j\in\mathcal{N}_i} \left[w_i - w_j - a_i(t) + a_j(t)\right]. \tag{25}$$

The computation of (25) requires only the virtual coordinates of UAV i and its neighbors. The virtual-coordinate dynamics are constructed as

$$\dot{w}_i = \mathrm{sat}_{[\dot{w}_{\min},\dot{w}_{\max}]}\left[v_w + \dot{a}_i(t) + k_w^c c_i + k_w^e e_{t,i}\right], \tag{26}$$

where $v_w > 0$ is the basic virtual-coordinate propagation speed, $k_w^c > 0$ is the distributed coordination gain, and $k_w^e > 0$ is the tracking-dependent propagation gain. Here $0 < \dot{w}_{\min} < \dot{w}_{\max}$, so the virtual coordinates propagate along the prescribed parameter direction with bounded rates. The feedforward term $\dot{a}_i(t)$ in (26) accounts for the variation in the desired tangential formation offset during formation reconfiguration. It is implemented as

$$\dot{a}_i(t_k) = \frac{a_i(t_{k+1}) - a_i(t_k)}{\Delta t}.$$

The term $k_w^e e_{t,i}$ couples the virtual-coordinate propagation with the physical tracking state and adjusts the propagation rate when the current UAV position and its individual reference point are not aligned in the tangential direction. The derivative $\dot{a}_i(t)$ compensates for changes in the desired tangential difference, whereas variations of $h_i(t)$ are handled by the position-reference feedback term in the inner layer.

3.3 Inner-Layer Guiding Vector Field and Local Repulsive Corrections

Based on the individual reference in (18) and the virtual-coordinate dynamics in (26), the inner-layer tracking field is constructed as

$$\boldsymbol{v}_i^{\mathrm{trk}} = \dot{w}_i \boldsymbol{f}_i'(w_i, t) - k_p \boldsymbol{e}_i, \tag{27}$$

where $k_p > 0$ is the position-reference tracking gain. The first term in (27) provides the propagation component along the individual parametric reference, whereas the second term provides the convergence component toward that reference.

Although the obstacle-aware path provides an obstacle-aware reference, a local obstacle repulsive term is further introduced according to the instantaneous UAV position. The clearance between UAV i and the enlarged boundary of obstacle m is defined as $d_{i,m}^b = \|\boldsymbol{p}_i - \boldsymbol{c}_m\| - r_m^b$. The corresponding activation coefficient is

$$\alpha_{i,m}^o = \mathrm{sat}_{[0,1]}\left(\frac{R_o - d_{i,m}^b}{R_o}\right),$$

where $R_o > 0$ is the effective range of the local obstacle correction. The obstacle repulsive velocity is defined as

$$\boldsymbol{v}_i^o = \sum_{m=1}^{M} k_o \left(\alpha_{i,m}^o\right)^2 \frac{\boldsymbol{p}_i - \boldsymbol{c}_m}{\|\boldsymbol{p}_i - \boldsymbol{c}_m\| + \varepsilon_p}, \tag{28}$$

where $k_o > 0$ is the obstacle-repulsion gain and $\varepsilon_p > 0$ is a small regularization constant.

To provide a local inter-UAV repulsive correction, define

$$\alpha_{ij}^c = \mathrm{sat}_{[0,1]}\left(\frac{R_c - \|\boldsymbol{p}_i - \boldsymbol{p}_j\|}{R_c}\right), \qquad j \neq i,$$

where $R_c > 0$ is the inter-UAV repulsion range. The corresponding repulsive velocity is

$$\boldsymbol{v}_i^c = \sum_{\substack{j=1 \\ j\neq i}}^{N} k_{\mathrm{col}} \left(\alpha_{ij}^c\right)^2 \frac{\boldsymbol{p}_i - \boldsymbol{p}_j}{\|\boldsymbol{p}_i - \boldsymbol{p}_j\| + \varepsilon_p}, \tag{29}$$

where $k_{\mathrm{col}} > 0$ is the inter-UAV repulsion gain.

The unsaturated velocity command is obtained by combining the inner-layer tracking field and the two local repulsive terms:

$$\overline{\boldsymbol{v}}_i = \boldsymbol{v}_i^{\mathrm{trk}} + \boldsymbol{v}_i^o + \boldsymbol{v}_i^c. \tag{30}$$

Finally, the velocity command applied to (1) is given by

$$\boldsymbol{v}_i = \begin{cases} \overline{\boldsymbol{v}}_i, & \|\overline{\boldsymbol{v}}_i\| \le v_{\max}, \\ \dfrac{v_{\max}\overline{\boldsymbol{v}}_i}{\|\overline{\boldsymbol{v}}_i\|}, & \|\overline{\boldsymbol{v}}_i\| > v_{\max}, \end{cases} \tag{31}$$

where $v_{\max} > 0$ denotes the maximum allowable velocity.

The two layers of the HGVF have complementary roles. The outer layer generates the obstacle-aware path, while the inner layer guides each UAV along its individual reference. The adaptive virtual-coordinate formation coordination mechanism changes the formation parameters and regulates the virtual-coordinate differences. The local repulsive terms modify the velocity command according to the instantaneous UAV–obstacle and inter-UAV distances. These terms provide local corrections rather than formal safety guarantees.

4 Experimental Results

4.1 Experimental Setup and Main Results

The proposed HGVF with adaptive virtual coordinates is evaluated using six UAVs connected by the cycle graph defined in Section 3.1. The simulation duration is 74 s, with a sampling interval of 0.02 s. The circular-formation radius is $R_f = 0.90$ m, and four static circular obstacles are placed

Table 3: Sensitivity analysis with respect to k_λ and A.

Sensitivity to k_λ						Sensitivity to A					
k_λ	$d_{\mathrm{o,min}}$	$d_{\mathrm{b,min}}$	$d_{\mathrm{u,min}}$	RMSE_p	RMSE_w	A	$d_{\mathrm{o,min}}$	$d_{\mathrm{b,min}}$	$d_{\mathrm{u,min}}$	RMSE_p	RMSE_w
0.65	0.6773	0.3273	0.073007	0.057648	0.0089835	1.25	0.62764	0.27764	0.043026	0.092898	0.014018
0.85	0.68567	0.33567	0.064039	0.061036	0.010252	1.5	0.66323	0.31323	0.056657	0.074691	0.012585
1.05	0.69247	0.34247	0.065303	0.065461	0.011804	1.75	0.69247	0.34247	0.065303	0.065461	0.011804
1.25	0.69828	0.34828	0.06811	0.069257	0.01316	2	0.72397	0.37397	0.070286	0.063524	0.011685
1.45	0.70587	0.35587	0.071149	0.0725	0.014322	2.25	0.75813	0.40813	0.064327	0.064845	0.012013

near the closed path. The enlarged obstacle boundaries use $d_b = 0.35\ \mathrm{m}$. Unless otherwise varied, $k_\lambda = 1.05$ and $A_m = A = 1.75$ for all obstacles.

Fig. 2a shows the localized normal deviations of the coarse manifold and the resulting multi-UAV formation motion. Although the coordination law uses only the cycle-graph neighbors, Fig. 2b evaluates the coordination errors of all 15 UAV pairs. The errors remain close to zero away from the obstacle-influence regions and temporarily increase during formation reconfiguration. The position-reference tracking errors in Fig. 3a also increase temporarily when the formation parameters and local repulsive corrections change, and then decrease toward zero. All obstacle clearances in Fig. 3b remain positive in this simulation. Figure 4 visualizes the corresponding multi-UAV motion sequence in CoppeliaSim.

4.2 Comparison and Parameter Sensitivity

The proposed method is compared with a velocity-based artificial potential field with consensus VAPF Ma et al. (2022) and an improved artificial potential field with leader–follower coordination APF Pan et al. (2022). The methods are evaluated using the same path, obstacles, number of UAVs, simulation duration, velocity bound, and initial conditions. Table 2 reports the minimum obstacle clearance $d_{\mathrm{o,min}}$, minimum enlarged-boundary clearance $d_{\mathrm{b,min}}$, minimum inter-UAV distance $d_{\mathrm{u,min}}$, position-reference tracking RMSE_p, and formation coordination RMSE_c. Each minimum is taken over the full evaluation interval and all relevant UAVs, obstacles, or UAV pairs.

The proposed method obtains the largest obstacle and enlarged-boundary clearances, $0.69982\ \mathrm{m}$ and $0.34982\ \mathrm{m}$, and the smallest position-reference tracking error, $0.094973\ \mathrm{m}$. VAPF–consensus maintains positive clearances but produces larger tracking and coordination errors. Improved APF–leader–follower obtains the largest inter-UAV distance and smallest coordination error, but its negative clearance values indicate penetration of both the obstacle and enlarged boundaries. In the considered comparison, the proposed method therefore improves obstacle clearance and position-reference tracking while maintaining a minimum inter-UAV distance of $0.27870\ \mathrm{m}$.

Table 3 examines k_λ and the common displacement amplitude $A_m = A$. Here, RMSE_w denotes the unscaled virtual-coordinate coordination error and is dimensionless. Increasing k_λ increases both clearances but also increases RMSE_p and RMSE_w. Increasing A generally increases the clearances, while both errors are smallest near $A = 2$.

5 Conclusion

This paper presented an HGVF with adaptive virtual coordinates for multi-UAV formation coordination around known static circular obstacles. The outer layer constructs an obstacle-aware path, while the obstacle-risk-dependent formation variable changes the virtual-coordinate offsets and normal offsets between circular and line formation parameters. The inner layer guides the UAVs along their individual references and incorporates local obstacle and inter-UAV repulsive corrections. Numerical results show positive obstacle clearances and temporary tracking and coordination deviations during formation reconfiguration. The baseline comparison and parameter sensitivity analysis further illustrate the effects on obstacle clearance, position-reference tracking, and virtual-coordinate coordination in the considered scenario.

REFERENCES

Javier Alonso-Mora, Tobias Naegeli, Roland Siegwart, and Paul Beardsley. Collision avoidance for aerial vehicles in multi-agent scenarios. *Autonomous Robots*, 39(1):101–121, 2015. doi: 10.1007/s10514-015-9429-0.

Aaron D. Ames, Xiangru Xu, Jessy W. Grizzle, and Paulo Tabuada. Control barrier function based quadratic programs for safety critical systems. *IEEE Transactions on Automatic Control*, 62(8): 3861–3876, 2017. doi: 10.1109/TAC.2016.2638961.

Hongda Chen, Kuo-Chu Chang, and Craig S. Agate. UAV path planning with tangent-plus-lyapunov vector field guidance and obstacle avoidance. *IEEE Transactions on Aerospace and Electronic Systems*, 49(2):840–856, 2013. doi: 10.1109/TAES.2013.6494384.

Soon-Jo Chung, Aditya A. Paranjape, Philip Dames, Shaojie Shen, and Vijay Kumar. A survey on aerial swarm robotics. *IEEE Transactions on Robotics*, 34(4):837–855, 2018. doi: 10.1109/TRO.2018.2857475.

Xiwang Dong, Yan Zhou, Zhang Ren, and Yisheng Zhong. Time-varying formation tracking for second-order multi-agent systems subjected to switching topologies with application to quadrotor formation flying. *IEEE Transactions on Industrial Electronics*, 64(6):5014–5024, 2017. doi: 10.1109/TIE.2016.2593656.

Zhixu Du, Hao Zhang, Zhuping Wang, and Huaicheng Yan. Model predictive formation tracking-containment control for multi-uavs with obstacle avoidance. *IEEE Transactions on Systems, Man, and Cybernetics: Systems*, 54(6):3404–3414, 2024. doi: 10.1109/TSMC.2024.3354893.

Vitor M. Goncalves, Luciano C. A. Pimenta, Carlos A. Maia, Bruno C. O. Dutra, and Guilherme A. S. Pereira. Vector fields for robot navigation along time-varying curves in n-dimensions. *IEEE Transactions on Robotics*, 26(4):647–659, 2010. doi: 10.1109/TRO.2010.2053077.

Iurii Kapitaniuk, Anton V. Proskurnikov, and Ming Cao. A guiding vector-field algorithm for path-following control of nonholonomic mobile robots. *IEEE Transactions on Control Systems Technology*, 26(4):1372–1385, 2018. doi: 10.1109/TCST.2017.2705059.

Oussama Khatib. Real-time obstacle avoidance for manipulators and mobile robots. *The International Journal of Robotics Research*, 5(1):90–98, 1986. doi: 10.1177/027836498600500106.

Xuejing Lan, Jianshuo Cai, Xiao-Meng Li, and Zhijia Zhao. Optimal cooperative fault-tolerant control for uav formation based on topology reconfiguration strategy. *IEEE Transactions on Aerospace and Electronic Systems*, 61(6):18743–18755, 2025. doi: 10.1109/TAES.2025.3615893.

Carlos E. Luis and Angela P. Schoellig. Trajectory generation for multiagent point-to-point transitions via distributed model predictive control. *IEEE Robotics and Automation Letters*, 4(2): 375–382, 2019. doi: 10.1109/LRA.2018.2890572.

Carlos E. Luis, Marijan Vukosavljev, and Angela P. Schoellig. Online trajectory generation with distributed model predictive control for multi-robot motion planning. *IEEE Robotics and Automation Letters*, 5(2):604–611, 2020. doi: 10.1109/LRA.2020.2964159.

Cheng Ma, Jinglei Li, Ying Shang, Shuai Zhang, and Qinghai Yang. A dynamic obstacle avoidance control algorithm for distributed multi-uav formation system. In *2022 IEEE International Conference on Mechatronics and Automation (ICMA)*, pp. 876–881, 2022. doi: 10.1109/ICMA54519.2022.9856064.

Farhad Mehdifar, Charalampos P. Bechlioulis, Farzad Hashemzadeh, and Mahdi Baradarannia. Prescribed performance distance-based formation control of multi-agent systems. *Automatica*, 119: 109086, 2020. doi: 10.1016/j.automatica.2020.109086.

Derek R. Nelson, D. Blake Barber, Timothy W. McLain, and Randal W. Beard. Vector field path following for miniature air vehicles. *IEEE Transactions on Robotics*, 23(3):519–529, 2007. doi: 10.1109/TRO.2007.898976.

Kwang-Kyo Oh, Myoung-Chul Park, and Hyo-Sung Ahn. A survey of multi-agent formation control. *Automatica*, 53:424–440, 2015. doi: 10.1016/j.automatica.2014.10.022.

Reza Olfati-Saber. Flocking for multi-agent dynamic systems: Algorithms and theory. *IEEE Transactions on Automatic Control*, 51(3):401–420, 2006. doi: 10.1109/TAC.2005.864190.

Zhenhua Pan, Chengxi Zhang, Yuanqing Xia, Hao Xiong, and Xiaodong Shao. An improved artificial potential field method for path planning and formation control of the multi-uav systems. *IEEE Transactions on Circuits and Systems II: Express Briefs*, 69(3):1129–1133, 2022. doi: 10.1109/TCSII.2021.3112787.

Wei Ren and Randal W. Beard. Consensus seeking in multiagent systems under dynamically changing interaction topologies. *IEEE Transactions on Automatic Control*, 50(5):655–661, 2005. doi: 10.1109/TAC.2005.846556.

Luis Ariel Valbuena Reyes and Herbert G. Tanner. Flocking, formation control, and path following for a group of mobile robots. *IEEE Transactions on Control Systems Technology*, 23(4):1268–1282, 2015. doi: 10.1109/TCST.2014.2363132.

Zhiyong Sun, Héctor García de Marina, Georg S. Seyboth, Brian D. O. Anderson, and Changbin Yu. Circular formation control of multiple unicycle-type agents with nonidentical constant speeds. *IEEE Transactions on Control Systems Technology*, 27(1):192–205, 2019. doi: 10.1109/TCST.2017.2763938.

Li Wang, Aaron D. Ames, and Magnus Egerstedt. Safety barrier certificates for collision-free multirobot systems. *IEEE Transactions on Robotics*, 33(3):661–674, 2017. doi: 10.1109/TRO.2017.2659727.

Yifan Wang and Xingyan Sun. Formation control of multi-uav with collision avoidance using artificial potential field. In *2019 11th International Conference on Intelligent Human-Machine Systems and Cybernetics (IHMSC)*, pp. 296–300, 2019. doi: 10.1109/IHMSC.2019.00075.

Yuanzhe Wang, Danwei Wang, and Senqiang Zhu. Cooperative moving path following for multiple fixed-wing unmanned aerial vehicles with speed constraints. *Automatica*, 100:82–89, 2019. doi: 10.1016/j.automatica.2018.11.004.

Wenlong Yang, Zongying Shi, and Yisheng Zhong. Distributed robust adaptive formation control of multi-agent systems with heterogeneous uncertainties and directed graphs. *Automatica*, 157:111275, 2023. doi: 10.1016/j.automatica.2023.111275.

Weijia Yao, Héctor García de Marina, Bohuan Lin, and Ming Cao. Singularity-free guiding vector field for robot navigation. *IEEE Transactions on Robotics*, 37(4):1206–1221, 2021. doi: 10.1109/TRO.2020.3043690.

Weijia Yao, Héctor García de Marina, Zhiyong Sun, and Ming Cao. Guiding vector fields for the distributed motion coordination of mobile robots. *IEEE Transactions on Robotics*, 39(2):1119–1135, 2023. doi: 10.1109/TRO.2022.3224257.

Yajing Yu, Chen Chen, Jian Guo, Mohammed Chadli, and Zhengrong Xiang. Adaptive formation control for unmanned aerial vehicles with collision avoidance and switching communication network. *IEEE Transactions on Fuzzy Systems*, 32(3):1435–1445, 2024. doi: 10.1109/TFUZZ.2023.3327114.

Shuai Zhang, Minjie Xu, and Xinhua Wang. Research on obstacle avoidance algorithm of multi-uav consistent formation based on improved dynamic window approach. In *2022 IEEE Asia-Pacific Conference on Image Processing, Electronics and Computers (IPEC)*, pp. 991–996, 2022. doi: 10.1109/IPEC54454.2022.9777606.

AI USE STATEMENT

Generative AI tools were used to assist with language polishing and the revision and debugging of experimental code. All methodological designs, mathematical derivations, experimental settings, results, and conclusions were independently reviewed and verified by the authors. The authors take full responsibility for the final content of this paper.